Nuclear pasta in hot dense matter and its implications for neutrino scattering

Alessandro Roggero[*]
Institute for Nuclear Theory, University of Washington, Seattle, Washington 98195, USA
and Theoretical Division, Los Alamos National Laboratory, Los Alamos, New Mexico 87545, USA

Jérôme Margueron[†]
Institute for Nuclear Theory, University of Washington, Seattle, Washington 98195, USA
and Institut de Physique Nucléaire de Lyon, CNRS/IN2P3, Université de Lyon, Université Claude Bernard Lyon 1, F-69622 Villeurbanne Cedex, France

Luke F. Roberts[‡]
National Superconducting Laboratory and Department of Physics and Astronomy, Michigan State University, East Lansing, Michigan 48824, USA

Sanjay Reddy[§]
Institute for Nuclear Theory, University of Washington, Seattle, Washington 98195, USA

(Received 27 October 2017; published 16 April 2018)

The abundance of large clusters of nucleons in neutron-rich matter at subnuclear density is found to be greatly reduced by finite-temperature effects when matter is close to β equilibrium, compared to the case where the electron fraction is fixed at $Y_e > 0.1$, as often considered in the literature. Large nuclei and exotic nonspherical nuclear configurations called pasta, favored in the vicinity of the transition to uniform matter at $T = 0$, dissolve at a relatively low temperature T_u as protons leak out of nuclei and pasta. For matter at β equilibrium with a negligible neutrino chemical potential we find that $T_u^\beta \simeq 4 \pm 1$ MeV for realistic equations of state. This is lower than the maximum temperature $T_{max}^\beta \simeq 9 \pm 1$ MeV at which nuclei can coexist with a gas of nucleons and can be explained by a change in the nature of the transition to uniform matter called retrograde condensation. An important new finding is that coherent neutrino scattering from nuclei and pasta makes a modest contribution to the opacity under the conditions encountered in supernovas and neutron star mergers. This is because large nuclear clusters dissolve at most relevant temperatures, and at lower temperatures, when clusters are present, Coulomb correlations between them suppress coherent neutrino scattering off individual clusters. Implications for neutrino signals from galactic supernovas are briefly discussed.

DOI: 10.1103/PhysRevC.97.045804

I. INTRODUCTION

The properties of hot dense matter encountered in core-collapse supernovas, newly born neutron stars called protoneutron stars, and neutron star mergers are expected to play a key role in shaping their observable photon, neutrino, and gravitational wave emission. In supernovas, state-of-the-art simulations indicate that neutrino transport at high densities influences the supernova mechanism [1,2], the long-term neutrino emission detectable in terrestrial neutrino detectors [3–6], and heavy-element nucleosynthesis [7–11].

The presence of heterogeneous matter at high densities is expected to modify the neutrino scattering rates because the size of structures encountered in such matter can be comparable to the neutrino wavelength, and neutrinos would couple coherently to the net weak charge contained within them. A familiar example is neutrino-nucleus coherent scattering, known to play an important role in trapping neutrinos during core collapse [12]. Additionally, heterogeneous phases are favored near first-order phase transitions in neutron stars at high densities [13], and coherent neutrino scattering in such matter can greatly increase the opacity [14]. Coherent neutrino scattering from the nuclear pasta phase, where large spherical and nonspherical nuclei coexist with a dense nucleon gas at densities between 10^{13} and 10^{14} g/cm^3, has also been studied [15,16].

Recently, the enhanced neutrino opacity in the high-density heterogeneous pasta phase was incorporated in simulations of protoneutron star evolution and found to have a significant impact on the temporal structure of the neutrino luminosity [17]. Motivated by this interesting finding, we perform calculations of matter at finite temperatures to address whether heterogeneous nuclear pasta is present under the typical thermodynamic conditions encountered in protoneutron stars and study its influence on the neutrino scattering rates. We find

[*]roggero@lanl.gov
[†]jmargue@uw.edu
[‡]robertsl@nscl.msu.edu
[§]sareddy@uw.edu

that the heterogeneous pasta phase dissolves at a relatively low temperature for the small values of the electron fraction characteristic of dense matter at β equilibrium. Consequently, the enhancement of neutrino scattering rates due to coherent scattering is relatively modest and significantly smaller than those employed in [17]. In addition, we find that Coulomb correlations between clusters suppresses scattering of neutrinos with wavelengths larger than the intercluster distance, in agreement with earlier work [18,19]. Interestingly, we also find that at lower temperatures where large nuclei can be present there could be a net reduction of the neutrino opacity as nucleons get locked up inside nuclei.

The material is organized as follows. In Sec. II we review the basic nuclear physics of phase coexistence and show that the simplified Gibbs construction for two-phase equilibrium provides a useful bound on the phase boundaries between homogeneous and heterogeneous matter. This allows us to provide an upper limit on the critical temperature above which pasta dissolves to form a uniform nucleon liquid, and its dependence on the nuclear equation of state is discussed. Implications for neutrino transport in protoneutron stars are discussed in Sec. III, and our conclusions are presented in Sec. IV.

II. HOT MATTER AT SUBNUCLEAR DENSITY AND THE DISSOLUTION OF PASTA

The structure of matter at subnuclear density and zero temperature is fairly well understood [20]. With increasing density, nuclei become neutron rich due to the rapid increase in the electron Fermi energy. Neutrons drip out of nuclei when the density exceeds $\rho_{\rm drip} \simeq 4 \times 10^{11}$ g/cm^3, and nonspherical or pasta nuclei are likely when the density exceeds $\rho_{\rm pasta} \simeq 10^{13}$ g/cm^3 [21]. Several studies using different many-body methods and underlying nuclear interactions have all yielded similar qualitative behavior [21–23].

At finite temperatures, the situation is less clear. Some calculations indicate that at the highest densities, nuclei and pasta persist up to $T \simeq 10$–15 MeV when the electron (or proton) fraction $\mathrm{Y_e} \gtrsim 0.1$ [24,25]. Others find that the large and coherent structures, such as rod, tubes, and planes, disappear at much lower temperatures [26,27].

In what follows we derive an upper bound on the temperature for the dissolution of nuclei and pasta for β-equilibrated matter at densities in the range $\rho \simeq 10^{12}$–10^{14} g/cm^3. We show that the dissolution of clusters is related to a change in the nature of the transition to the high-density uniform phase, which turns from an ordinary gas-to-liquid transition, during which the volume fraction of the high-density phase continues to increase, into a less ordinary gas-to-liquid-to-gas transition, also called retrograde condensation, where the volume fraction of the high-density phase decreases [28]. To begin we consider β-equilibrium matter with zero neutrino chemical potential because the outer regions of a protoneutron star, which may contain nuclear pasta, are able to deleptonize rapidly and reach β equilibrium on a short timescale compared to the timescales of relevance to protoneutron star evolution [3–6].

First, we identify the thermodynamic conditions favorable for the existence of nuclear pasta. Since surface and Coulomb energies act to disfavor the heterogeneous state, and shell effects are relatively small at the temperatures of interest, the liquid-gas phase coexistence region predicted by the Gibbs construction, where these effects are ignored, will likely enclose the phase coexistence region predicted when such finite-size effects are included. This simple observation allows us to provide a useful upper bound on the dissolution temperature by examining the two-phase Gibbs construction for bulk matter. We note that neglecting finite-size effects has been shown to provide results comparable to those with the Thomas-Fermi approach at finite temperatures [29] (see the Erratum to this reference), as well as those obtained from a quantum molecular dynamics calculation [27].

In the following, we briefly recall the well-known Gibbs construction applied to a nuclear system composed of neutrons and protons [25,28,30]. For nuclei or pasta to coexist with a gas of nucleons, the high-density liquid phase inside these structures has to be at equilibrium with the low-density gas outside. Denoting the pressure and the neutron and proton chemical potentials of the high-density liquid phase P^h, μ_n^h, and μ_p^h, respectively, Gibbs equilibrium requires $P^h = P^l$, $\mu_n^h = \mu_n^l$, and $\mu_p^h = \mu_p^l$, where P^l, μ_n^l, and μ_p^l, are the corresponding pressure and chemical potentials in the low-density gas phase. To find the coexistence region in the phase diagram an equation of state (EOS) which specifies how the energy density of bulk nucleonic matter $\varepsilon_{\rm nuc}(n_n,n_p,T)$ depends on the neutron and proton densities and the temperature is needed. In practice we work in the proton-canonical ensemble where μ_n is fixed and n_p is the extensive variable [30]. We have, however, checked that our results are independent of the statistical ensemble.

At a fixed temperature, phase coexistence is possible when there exist two pairs of nucleon densities, denoted n_n^h, n_p^h and n_n^l, n_p^l, that can satisfy the Gibbs equilibrium criteria. These pairs can be depicted as two points in a two-dimensional plot where the axes are the neutron and proton densities. In Fig. 1 these points are calculated for the model SLy4 and appear on the solid black curve. For a pair of points at Gibbs equilibrium, a Gibbs construction can be used to find the state of matter at intermediate densities. Therefore, a pair of points that satisfy Gibbs equilibrium defines a curve through the neutron-proton density space given by [31]

$$\begin{aligned} n_n &= u n_n^h + (1-u) n_n^l, \\ n_p &= u n_p^h + (1-u) n_p^l, \end{aligned} \tag{1}$$

where u is the fraction of the volume that is occupied by the high-density liquid phase. The thin purple curves represent these curves for pairs of select Gibbs equilibrium points. For example, in Fig. 1(b), the pair of end points defined by the intersection labeled "l" and "h" specifies the neutron and proton densities of the low- and high-density phases, n_n^l, n_p^l and n_n^h, n_p^h, respectively. Clearly, Y_e varies along any Gibbs construction curve, so a constant Y_e curve crosses the Gibbs constructions of many Gibbs equilibrium pairs in the mixed-phase region. In Fig. 1, the dashed yellow lines show curves of constant Y_e and the Gibbs equilibrium at a specific Y_e is defined by its intersection with the purple curve. The thick blue curve denotes the β-equilibrium path, along which $\mu_n - \mu_p = \mu_e$. Gibbs equilibrium is possible along the β-equilibrium path when the thick blue curve lies within

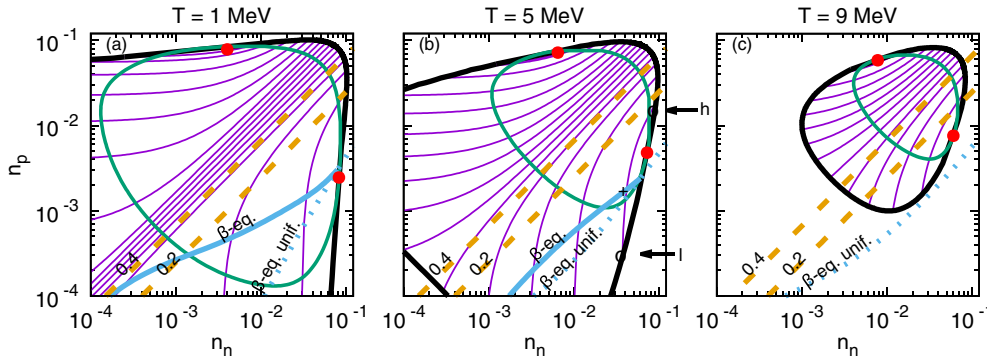

FIG. 1. β-equilibrium path (thick solid blue line) for SLy4 Skyrme interaction in the coexistence region (delimited by the thick solid black line) in the (n_n, n_p) plane and for $T = 1$–9 MeV. A sample of the Gibbs construction paths is shown (thin solid purple lines). The global density, which intersects the β-equilibrium path line with the Gibbs construction one (see, for instance, the "+"symbol at $T = 5$ MeV), represents the equilibrium state connecting the two phases at equilibrium which are located at the boundaries (see the points labeled "l" and "h," which are the low- and high-density phases associated with the global density identified by the + symbol at β equilibrium). The constant $Y_e = 0.2$, 0.3, and 0.4 paths are represented by the thick dashed yellow lines. The spinodal instability region is also shown (thin solid green line) and the critical points are shown by filled red circles with error bars.

the coexistence region. Once again, it can be seen that the β-equilibrium curve moves across many Gibbs equilibrium pairs as it traverses the coexistence region. The β-equilibrium path for the homogeneous phase is also shown as the dashed blue curve for reference. The spinodal region where matter is unstable to small density perturbations is the region enclosed by the thin green curve, and the critical points associated with the first-order transition are denoted by the filled red circles.

Several insights about the role of finite temperature can be gleaned from examining the progression of the phase coexistence region with temperature shown in Figs. 1(a)–1(c).

(1) With increasing temperature the extent of the phase coexistence region shrinks, and its intersection with the path of β equilibrium decreases. Above the critical temperature, $T^{\beta}_{\rm max}$ ($\simeq 9$ MeV for the model chosen), there is no intersection and phase coexistence at β equilibrium is not possible.

(2) In contrast, out of β equilibrium for moderate values of $Y_e > 0.2$ there exists a range of ambient conditions that extends to higher temperatures where Gibbs equilibrium is possible. Nonetheless, with increasing temperature the area enclosed by the solid black coexistence curve shrinks and its intersection with lines of constant Y_e is reduced. Eventually, above the critical temperature denoted $T^{Y_e}_{\rm max} \simeq 12$–15 MeV there is no intersection and phase coexistence is absent.

(3) Coexistence at β equilibrium ends near the critical point. With increasing temperature, phase coexistence ends by making a transition to the uniform low-density gas phase. This feature, called retrograde condensation [28], implies that the path along β equilibrium will favor fewer nuclei with increasing density.

(4) For moderate values of $Y_e > 0.2$ phase coexistence ends by transiting to the high-density liquid phase and large nuclei persist to higher temperatures.

(5) With increasing temperature, the density contrast between the high- and the low-density phases associated with Gibbs equilibrium is reduced.

The impact of retrograde condensation on the volume fraction of the high-density liquid phase is shown more clearly in Fig. 2. At low temperatures, u begins close to 0 at low densities and increases to 1 at high densities, implying that it exits the coexistence region in the high-density phase. But above a critical temperature, u reaches a maximum of less than 1 and turns over, implying that the β-equilibrium path exits the coexistence region in the low-density gas phase. The fact that the maximum volume fraction occupied by the high-density phase, which corresponds to nuclei or pasta structures, is rather small at temperatures high enough for retrograde condensation can significantly impact the contribution of coherent scattering to the neutrino opacity of β-equilibrium matter. Since non-spherical shapes or pasta nuclei are favored for $u \gtrsim 1/8$ (for a pedagogic discussion of pasta nuclei see Ref. [21]) we include the dashed horizontal line at $u = 1/8$ to help extract the critical

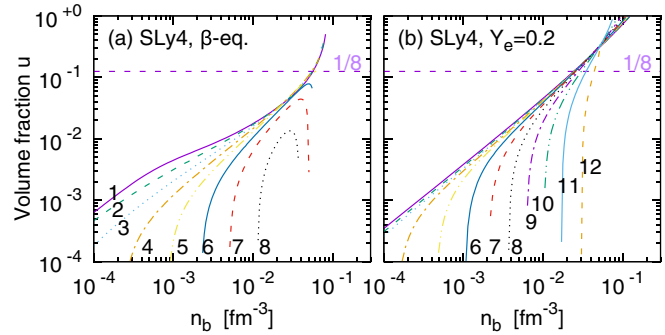

FIG. 2. Volume fraction of the high-density phase in heterogeneous matter for SLy4 Skyrme interaction. (a) For the β-equilibrium path; (b) for the constant $Y_e = 0.2$ path.

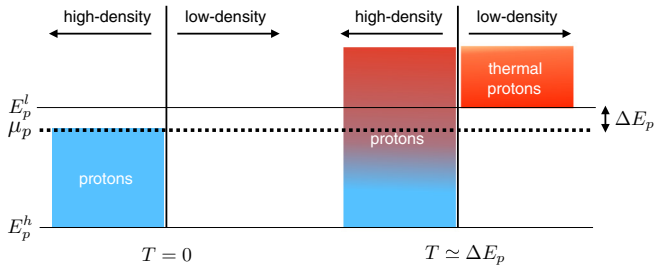

FIG. 3. This schematic shows the occupied proton energy levels in the low- and high-density phases that coexist in the heterogeneous phase. The $T = 0$ situation is shown at the left, and the finite temperature at which a significant thermal population exists in the low-density phase is shown at the right. See text for additional details.

temperature T_u^β above which pasta nuclei no longer appear (note that $T_u^\beta < T_{\rm max}^\beta$). In Fig. 2(a) we see that T_u^β is between 5 and 6 MeV (for SLy4 EOS). In contrast for matter at fixed $Y_e = 0.2$, shown in Fig. 2(b), pasta nuclei persist to higher temperatures until phase coexistence ends at $T_{\rm max}^{Y_e}$

We can understand the physical mechanism for retrograde condensation at higher temperatures by examining the evolution of the proton fraction in the gas phase. Global charge neutrality ($n_e = n_p$) and Eq. (1) require the volume fraction of the high-density phase to be

$$u = \frac{n_e - n_p^l}{n_p^h - n_p^l}, \tag{2}$$

where the electron density n_e is assumed to be uniform because the Debye screening length is large compared to the typical size of electrically neutral Wigner-Seitz cells. In the β-equilibrium mixed phase the lowest energy level for protons in the low-density gas phase $E_p^l > \mu_p$, and at $T = 0$ the proton density there is denoted $n_p^l = 0$. At $T = 0$ the volume fraction $u = n_e/n_p^h$ increases rapidly with increasing density because n_e increases and n_p^h decreases. At finite temperature $n_p^l > 0$ because proton states in the gas can be thermally populated. This is illustrated in Fig. 3, where the occupied energy levels of protons in both the low- and the high-density phases are shown at zero and finite temperature.

The thermal population of protons in the gas [31]

$$n_p^l \simeq 2\left(\frac{m_p T}{2\pi}\right)^{3/2} e^{-\Delta E_p/T}, \tag{3}$$

where $\Delta E_p = E_P^l - \mu_p$, becomes significant when $T \simeq \Delta E_p$ and increases exponentially with temperature. In contrast, the density of protons in the high-density phase remains significantly higher and does not change appreciably with temperature because of their high degeneracy.

The typical evolution of $\Delta E_p/T$ is shown in Fig. 4(a) for the SLy4 EOS. Except close to the transition density, $\Delta E_p/T \gg 1$ leads to significant suppression of the proton density in the gas phase. In the vicinity of the transition density $\Delta E_p/T$ decreases rapidly and from Eq. (3) the proton fraction in the gas increases exponentially. The number densities of the charged particles as a function of the average baryon density are shown in Fig. 4(b). Since electric charge neutrality in the uniform

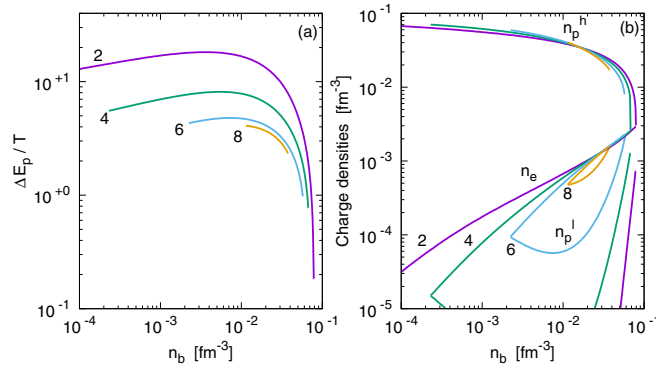

FIG. 4. (a) Energy differences $\Delta E_p/T$ and (b) charge particle densities (n_e, n_p^l, n_p^h) as a function of the density at different temperatures $T = 1$–6 MeV. The SLy4 EOS is considered here.

phase requires $n_e = n_p = n_p^{\rm gas}$, the point at which n_e and n_p^l first intersect defines the low-density boundary of the coexistence region. In the vicinity of this point, nonuniform matter is predominantly composed of the gas phase. The high-density boundary is defined by the intersection of the n_e and n_p^h at low temperatures or by the second intersection of the n_e and n_p^l at high temperatures as expected for retrograde condensation. These features are also readily discernible in Fig. 2, where the evolution of the volume fraction of the high-density phase with the density is shown for various temperatures.

As expected from the preceding discussion and Eq. (2), for matter at β equilibrium where Y_e is small, the volume fraction u will decrease with the density for $T \gtrsim \Delta E_p$. When this criterion is met, the density of protons in the low-density gas phase will become comparable to the electron density, and eventually as ΔE_p decreases with density the volume fraction $u \to 0$.

We now turn to study of the model dependence of the critical temperatures denoted T_m^β, $T_{\rm max}^\beta$, and $T_{\rm max}^{Y_e}$, discussed earlier. We first select a subset of model Skyrme and relativistic mean-field EOSs that predict the energy per particle of neutron matter at $n_b = 0.06$ and 0.10 fm^{-3}, which are compatible with the quantum Monte Carlo [32] or many body perturbation theory (MBPT) [33], which are based on two- and three-body chiral effective field theory (EFT) potentials. The pasta dissolution temperatures T_u^β for these models are shown in Fig. 5(a). The names of the EOSs are shown vertically above the predictions and the EOSs are ordered according to the slope of the symmetry energy at nuclear saturation density, denoted $L_{\rm sym}$. The average prediction is $T_u^\beta = 5.0 \pm 2$ MeV and decreases with $L_{\rm sym}$ (the anticorrelation coefficient is -0.81) and the dispersion reflects the additional dependence on the EOS parameters. In Fig. 5(b) we show the highest average density of the coexistence region associated with T_u^β and $T_{\rm max}^{Y_e=0.4}$ for the EOSs in Fig. 5(a) and find that they are clearly anticorrelated with $L_{\rm sym}$.

The striking feature here is that the pasta dissolution temperature at β equilibrium is much lower than the maximal temperature of the phase coexistence and that the maximal temperature $T_{\rm max}^{Y_e}$ even at a modest value of $Y_e = 0.2$ is about a factor of 2 higher than T_u^β. For typical values of $L_{\rm sym}$, around

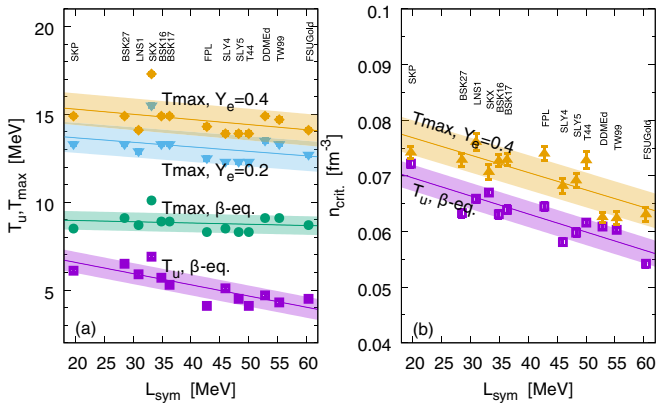

FIG. 5. (a) Dissolution temperature $T_{\rm u}$ and maximal temperatures $T_{\rm max}$ at β equilibrium, compared to $T_{\rm max}$ at fixed $x_e = 0.2$ and 0.4 for the set of EOSs compatible with the chiral EFT EOS in neutron matter. (b) Highest density reached by the pasta phase for β equilibrium or at fixed Y_e. These predictions are shown versus $L_{\rm sym}$.

50–60 MeV, the dissolution temperature is estimated to be $T_u^\beta \simeq 4 \pm 1$ MeV. Since our analysis neglects finite-size effects such as surface, Coulomb, and shell effects we believe that this is an upper limit on the dissolution temperature.

It is interesting to compare our predictions with those of other works. The maximal temperature at fixed electron fraction $Y_e = 0.3(0.5)$ was estimated from a quantum molecular dynamics simulation to be about 5(6) MeV [26]. In a similar approach and fixing $Y_e = 0.3$, the maximal temperature was found to be 6 and 9 MeV for two nuclear EOSs with $L_{\rm sym} = 93$ and 80 MeV [27]. In addition, another temperature scale was introduced: the temperature at which the nuclear surface is blurred due to proton drip-out. This characteristic temperature is qualitatively similar to the dissolution temperature T_u in our approach. It was estimated to be around 3 MeV in Ref. [26] and around 3 or 4 MeV, depending on the nuclear EOS, in Ref. [27]. These two temperature scales are lower than ours, confirming that our temperature scales shown in Fig. 5 represent upper bounds. Note also that the values of $L_{\rm sym}$ of these nuclear EOSs are significantly larger than the ones we considered, and our results imply that the larger the value of $L_{\rm sym}$, the lower the temperature (see Fig. 5). This also contributes in part to explaining the differences between our results and those of the quantum Monte Carlo approach. Due to its computationally heavy framework, an extended model dependence of quantum molecular dynamics in the nuclear EOS has not yet been done. A more systematic study was done based on a Thomas-Fermi approach, and the pasta phase in β-equilibrium matter was shown to melt above 5–6 MeV [34]. This again is lower than our estimate for the maximal temperature, as expected. Finally, a recent quantum calculation (Hartree-Fock) has been performed, confirming that our estimate of T_u^β is an upper limit for the melting of the crust [35].

III. NEUTRINO SCATTERING

Coherent neutrino scattering from nuclei and pasta can be estimated using the two-phase Gibbs construction discussed in the preceding section if their typical size is known. The nuclear size is set by the competition between the surface and the Coulomb energies, mass number, and charge of the energetically favored nuclei can be calculated by specifying the surface tension [21]. Shell effects can also play a role but we can expect their impact to be less important at the temperatures of interest, and we neglect them in the following analysis. Further, although we should expect a distribution of nuclei at finite temperature, to obtain a simple first estimate we assume that the distribution is dominated by a single nucleus. In this case, the radius of the favored nucleus is [21]

$$r_A^3 = \frac{3\sigma}{4\pi e^2 \left(n_p^h\right)^2 f_3(u)} \quad \text{with} \quad f_3(u) = \frac{2 - 3u^{1/3} + u}{5}, \tag{4}$$

where σ is the surface tension between the low- and the high-density phases, and $f_3(u)$ is the geometrical factor associated with the Coulomb energy of the Wigner-Seitz cell in $d = 3$ dimensions [36]. The surface tension is a function of the density, Y_e, and T. We use the ansatz from Ref. [37] (see also Ref. [38]) and parameters obtained for the SLy4 interaction. Note that this simple ansatz neglects the influence of the protons in the low-density gas phase on the surface tension [39].

For the purpose of calculating coherent neutrino scattering, we, for simplicity, assume that nuclei are spherical for all values of u. This is reasonable because angle-averaged coherent scattering rates from rodlike and slablike structures have been calculated earlier and found to be comparable to or smaller than those from spherical nuclei of similar size [40]. Further, as noted earlier, close to β equilibrium the pasta region is relatively small even for $T < T_{\rm u}^\beta$ and absent for $T > T_{\rm u}^\beta$.

The differential coherent elastic scattering rate from the nuclei in the heterogeneous phase is given by [14,41]

$$\frac{d\Gamma_{\rm coh}}{d\cos\theta} = \frac{G_F^2 E_\nu^2}{8\pi} n_A (1 + \cos\theta) S(q) N_{\rm w}^2 F_A^2(q), \tag{5}$$

where the total weak charge of a nucleus is defined as [14]

$$N_{\rm w} = \frac{4\pi}{3} r_A^3 \left(n_n^h - n_n^l\right), \tag{6}$$

and $n_A = 3u/(4\pi r_A^3)$ is the density of nuclei. We have neglected the proton contribution in the vector response because of their weak charge, $\simeq 1 - 4\sin^2\theta_W \approx 0$, and subtracted the density of neutrons from the low-density phase because neutrinos only scatter off the density contrast. The static structure factor $S(q)$ accounts for correlations between nuclei due to long-range Coulomb interactions (weakly screened by electrons), which tend to suppress scattering at small momentum transfer $q = E_\nu\sqrt{2(1-\cos\theta)} \lesssim 1/a$, where $a = (3/4\pi n_A)^{1/3} = r_A/u^{1/3}$ is the average distance between nuclei. Scattering with high momentum transfer at $q \gtrsim 1/r_A$ is suppressed by the form factor of the nucleus $F_A(q)$, which we take to be that of a sphere of constant density and radius r_A. More realistic choices, such as the Helm form factor [42], have a negligible impact on our results.

In a one-component plasma, $S(q)$ depends on a and the Coulomb coupling parameter $\Gamma = Z^2 e^2/a k_B T$, where Z is the ion charge, $e^2 = 1/137$, and $k_B T$ is the thermal energy. In our simple model for the heterogeneous state where we assume

that a single spherical nucleus captures the essential physics and ^{56}Fe is the ground state at zero density,

$$Z \approx 26\left(\frac{\sigma}{\sigma_0}\right)\left(\frac{n_0}{2n_p^h}\right)\left(\frac{f_3(0)}{f_3(u)}\right), \tag{7}$$

where we have used Eq. (4) and the following parameters: $\sigma_0 \simeq 1.2$ MeV/fm^2 is the surface tension of symmetric nuclei in vacuum, and $n_0 \simeq 0.16$ fm^{-3} is the nuclear saturation density. Typically we find $Z \simeq 50$ at the density for which we expect an appreciable fraction of large nuclei or pasta, and $\Gamma \gg 1$. For large Γ the static structure factor $S(q) \ll 1$ unless $qa \gg 1$, and for $\Gamma > 10$ the interference of amplitudes for neutrino scattering off different clusters is strong and destructive at small $qa <$ 2–3. At intermediate $qa \simeq$ 4–5, constructive interference can enhance scattering, and for $qa \gg 5$, where interference is negligible, $S(q) \simeq 1$. In this work we employ $S(q)$ obtained from recent fits to accurate molecular dynamics simulations of one-component plasmas [43] to properly account for screening for Γ in the range 1–150. We note that for $T > 2$ MeV, $\Gamma < 150$ even at the highest density, crystallization is not favored, and it is reasonable to work with $S(q)$ obtained for the liquid state.

The neutrino scattering rate from nonrelativistic nucleons in the gas phase is given by [45]

$$\frac{d\Gamma_\nu}{d\cos\theta} = \frac{G_F^2 E_\nu^2}{8\pi}\sum_{ij}\left[(1+\cos\theta)C_v^i C_v^j S_v^{ij}(q) + (3-\cos\theta)C_a^i C_a^j S_a^{ij}(q)\right], \tag{8}$$

where the labels i and j can be either neutrons or protons, and C_v^i and C_a^i are their corresponding vector and axial vector charges. In the long-wavelength limit, which is adequate to describe low-energy neutrino scattering, the static structure factors (unnormalized) can be related to thermodynamic functions [31],

$$S_v^{ij} = T\left(\frac{\partial^2 P}{\partial\mu_j\partial\mu_i}\right)_T, \tag{9}$$

where P is the pressure of the gas phase and μ_i is the chemical potential of either neutrons or protons, and the axial or spin response,

$$S_a^{ij} = T\left(\frac{\partial^2 P}{\partial\delta_j\partial\delta_i}\right)_T, \tag{10}$$

where δ_i is the chemical potential associated with the spin density of species i. When interactions between nucleons can be neglected, the structure functions greatly simplify and are given by

$$S_v^{ij} = S_a^{ij} = \delta^{ij} S_{\rm gas}(\mu_i, T), \tag{11}$$

where [44]

$$S_{\rm gas}(\mu_i, T) = \int \frac{d^3p}{(2\pi)^3}\frac{e^{\beta(p^2/2m-\mu_i)}}{(1+e^{\beta(p^2/2m-\mu_i)})^2}, \tag{12}$$

where $\beta = 1/T$ and only correlations due to Fermi statistics are included. Strong nuclear interactions induce additional correlations between nucleons in the gas and can alter the structure factors. At the subnuclear densities of interest, calculations suggest a modest enhancement of the vector response and a suppression by up to 50% of the axial response [45–49]. Since our primary interest here is to assess the role of coherent scattering, in what follows we neglect corrections due to strong interactions and use Eq. (11) to calculate the scattering rates in the gas phase.

To assess the importance of coherent scattering from heavy nuclei in the heterogeneous phase we define the ratio

$$\mathcal{R} = \frac{\sigma_{\rm het}^{\rm tran}(E_\nu)}{\sigma_{\rm hom}^{\rm tran}(E_\nu)} = \frac{\sigma_{\rm coh}^{\rm tran}(E_\nu)+\sigma_{\rm gas}^{\rm tran}(E_\nu)}{\sigma_{\rm hom}^{\rm tran}(E_\nu)} = \frac{n_A N_{\rm w}^2\langle S_{\rm cl}(E_\nu)\rangle + \left(1+5\left(C_A^n\right)^2\right)S_{\rm gas}\left(\mu_n^{\rm het},T\right)+5\left(C_A^p\right)^2 S_{\rm gas}\left(\mu_p^{\rm het},T\right)}{\left(1+5\left(C_A^n\right)^2\right)S_{\rm gas}\left(\mu_n^{\rm hom},T\right)+5\left(C_A^p\right)^2 S_{\rm gas}\left(\mu_p^{\rm hom},T\right)}, \tag{13}$$

where $\sigma^{\rm tran} = \int d\cos\theta(1-\cos\theta)d\Gamma/d\cos\theta$ is the elastic transport cross section per unit volume for neutrinos. $\mathcal{R}$ is analogous to the parameter ξ introduced in [17] and quantifies the change in neutrino scattering rates in the heterogeneous phase, where both coherent scattering from nuclei ($\sigma_{\rm coh}^{\rm tran}$) and scattering from free nucleons in the gas phase contribute. The term $\langle S_{\rm cl}(E_\nu)\rangle$ in the cross section from clusters indicates angle averaging of the corrections due to correlations and nuclear form factors [17],

$$\langle S_{\rm cl}(E_\nu)\rangle = \frac{3}{4}\int_{-1}^{1} d\cos\theta(1-\cos\theta)(1+\cos\theta)S(q)F_A^2(q), \tag{14}$$

and is a function of E_ν though $q = E_\nu\sqrt{2(1-\cos\theta)}$. We note that neglecting the correlations in both the gas and the protons has a small impact, $\lesssim$10%, on the ratio. However, a strong suppression of the nucleon axial response due to spin correlations would reduce the opacity of the homogeneous phase and favor larger $\mathcal{R}$.

The results for the ratio of cross section $\mathcal{R}$ are displayed in Fig. 6. Figure 6(a) shows results at fixed proton fraction $Y_e = 0.4$, and Fig. 6(b) results for matter at β equilibrium. In both cases, with the exception of the dashed black line, neutrinos are assumed to be thermal and their energy $E_\nu = 3T$. The energy dependence of the cross sections is shown in Fig. 7. The strong suppression of coherent scattering at low energy is clearly visible, and the circle on each curve corresponding to $E_\nu = 3T$ shows that Coulomb correlation suppresses scattering for neutrino energies of interest. The Coulomb parameter Γ for the plots in Fig. 7 range from $\Gamma_{\rm min} = 4(6)$ for $n_B = 0.01$ fm^{-3} and $T = 10(6)$ MeV to $\Gamma_{\rm max} = 150(74)$ for $u = 1/8$ and $T = 1$ MeV at fixed proton fraction (β equilibrium). The value of Γ at select points is

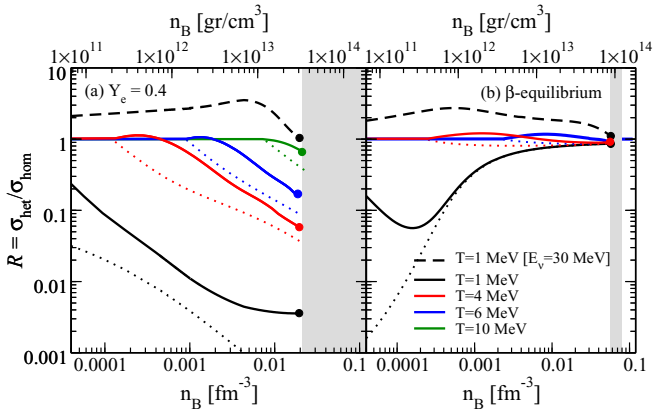

FIG. 6. Ratio $\mathcal{R}$ from Eq. (13) under two conditions: (a) fixed proton fraction $Y_e = 0.4$ and (b) β equilibrium. The gray central band indicates the density region where nonspherical pasta may be present, and the curves terminate in a circle at the density at which $u = 1/8$. Dotted curves indicate the contribution of the external gas only. Neutrinos are considered to be at thermal equilibrium, except for the dashed black curves, where $E_\nu = 30$ MeV.

reported in Table I. At the lowest temperature, $T = 1$ MeV, and the large proton fraction $Y_e = 0.4$, our simple ansatz in Eq. (7) predicts a large $Z > 60$ and $\Gamma > 200$. At these very low temperatures, it would be appropriate to use $S(q)$ from simulations of the solid phase. However, here we adopt the approximate treatment suggested in earlier studies [19,50] where they circumvent the problem by limiting the value of the Coulomb coupling to $\Gamma_{\max} = 150$, which is indicated by an asterisk in Table II. These low-temperature conditions are encountered only at late times in the protoneutron star phase when the neutrino luminosity is greatly reduced and undetectable even for nearby supernovas in detectors such as SuperKamiokande, where the energy threshold is about 5 MeV. Additionally, shell effects can be important in the determination of Z at low temperatures, and smaller values of $Z \approx 40$–50 are obtained at $T = 0$ [22,51]. Nonetheless,

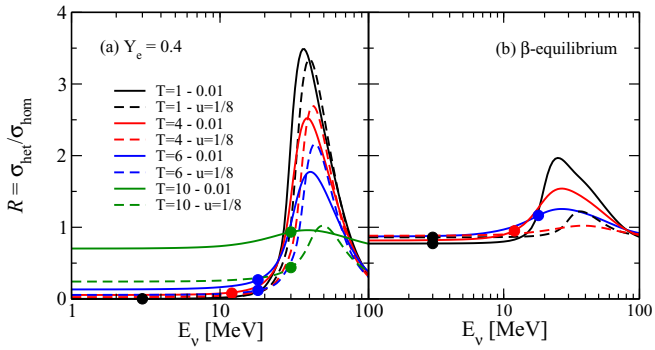

FIG. 7. Energy dependence of the total ratio of cross section $\mathcal{R}$ at various temperatures and for two densities: $n_B = 0.01$ fm^{-3} (solid lines) and the threshold density at which $u = 1/8$ (dashed lines). As for Fig. 6, (a) shows results for a fixed proton fraction $Y_e = 0.4$, and (b) for β-equilibrium conditions. In both cases the filled circles indicate the energies for thermal neutrinos ($E_\nu = 3T$).

TABLE I. Values of neutrino mean-free-path and diffusion coefficients at $T = 4$ MeV and $n_B = 0.01$ fm^{-3}.

	$Y_e = 0.4$		β	
	Hom	Het	Hom	Het
λ ($E_\nu = 3T$) (m)	14.91	98.03	14.19	14.87
D_2 (m)	67.01	575.01	63.77	74.47
D_4 (m)	220.79	1326.91	210.12	208.71

we included these low-temperature results, which, despite the approximations mentioned, provide useful insights about trends and allow for comparison with earlier work.

A related quantity of interest for neutrino transport are the diffusion coefficients

$$D_n = \int_0^\infty dx x^n \lambda(E_\nu) f(E_\nu)[1 - f(E_\nu)], \qquad (15)$$

with $x = E_\nu/T$ and f the Fermi-Dirac distribution [4]. Results for D_2 and D_4 at $T = 4$ MeV and $n_B = 0.01$ fm^{-3} for both β equilibrium and fixed $Y_e = 0.4$ are presented in Table II, assuming that the neutrino chemical potential μ_ν is negligible. In the first row of data we also list the result for the mean free path $\lambda(E_\nu) = 1/\sigma(E_\nu)$ at $E_\nu = 3T$. These results are compatible with the general trend observed in the results above that predict small effects of pasta at β equilibrium and reduced scattering at a fixed proton fraction.

From Figs. 6 and 7 we can draw the following conclusions.

(1) At low temperatures, when large nuclei are present and persist up to high densities, the opacity to high-energy neutrinos with $E_\nu \gtrsim 4/a$, where a, the distance between nuclei, is enhanced, but coherent scattering is greatly reduced for low-energy thermal neutrinos due to Coulomb correlations between nuclei. We find a net reduction in the scattering rates in the heterogeneous phase because a large fraction of free nucleons is tied up inside nuclei. In the homogeneous phase these nucleons make a significant contribution to neutrino scattering because they couple to the axial current.

(2) At β equilibrium coherent scattering makes a relatively small contribution to the total neutrino opacity for all temperatures of interest. At low temperatures, when nuclei and pasta are present, Coulomb correlations reduce coherent scattering, and at high temperatures, pasta and large nuclei melt. We find that scattering off nucleons in the gas phase dominates unless nuclear

TABLE II. Values of Coulomb coupling Γ for Fig. 7.

T (MeV)	$Y_e = 0.4$		β	
	$n_B = 0.01$	$u = 1/8$	$n_B = 0.01$	$u = 1/8$
1	150*	150*	72.7	74.0
4	69.8	138.8	14.2	4.0
6	35.1	75.4	6.3	–
10	4.0	17.4	–	–

correlations can greatly suppress the spin response of dilute nuclear matter.

(3) The large opacity due to coherent scattering reported in Ref. [17] arose because the neutrino energy was chosen to be high to ensure that the suppression due to Coulomb correlations was mild, and it was assumed that pasta nuclei would survive up to $T \simeq 10$ MeV in matter close to β equilibrium.

(4) Figure 7 illustrates that the heterogeneous phases can act as a low-pass filter for neutrinos. In the diffusive regime the strong energy dependence of the neutrino cross sections would imply nonlinear thermal evolution where cooling would accelerate rapidly with decreasing temperature.

These results have significant implications for the impact of coherent pasta scattering on protoneutron star cooling. In Ref. [17], it was shown that if coherent scattering from nuclear pasta increases the neutrino opacity relative to that of a homogeneous gas, pasta formation in the outer layers of the protoneutron star can trap neutrino energy for the first few seconds after a successful core-collapse supernova explosion. This heat trapping causes the temperature of the outer layers of the protoneutron to increase until they reach the pasta melting temperature. This heats up the entire region over which neutrinos decouple from matter, increasing the average energy of neutrinos escaping from the protoneutron star. Additionally, the energy that is trapped initially gets out at later times. Both of these effects contributed to a more detectable late-time neutrino signal. A pasta melting temperature of 10 MeV was used in their parameterized simulations, but it was suggested that reducing the melting temperature of the pasta could reduce the impact of the pasta on the neutrino signal.

Here, we have found that the pasta dissolution temperature for β-equilibrated matter is $T_{\rm u}^{\beta} \approx 4 \pm 1$ MeV and that the presence of a high-density phase can reduce the neutrino opacity. First, this implies that even if coherent scattering from nuclear pasta increased the neutrino opacity, the impact of pasta on the protoneutron star neutrino signal would be smaller than the impact predicted by Ref. [17], since nuclear pasta would be present for a shorter portion of the protoneutron star cooling. The reduced melting temperature would also cause a smaller perturbation in the temperature gradient near the neutrino sphere, which would reduce the enhancement of the neutrino luminosity even when the pasta is present. Second, we predict that correlations among high-density structures act to reduce the neutrino opacity for neutrinos with energies $\lesssim 4/a$, which is an energy scale that is often significantly above the thermal energy. Therefore, the presence of pasta may allow the majority of thermal neutrinos to escape more easily and potentially speed up neutrino cooling, thereby reducing the late-time neutrino detection rate from a nearby supernova.

IV. CONCLUSIONS

In this paper, we have analyzed the properties of the hot nuclear pasta phase and we have shown the large qualitative differences between matter at β equilibrium and matter at a modest electron fraction, $Y_e > 0.2$. At β equilibrium, we find that pasta melts or dissolves at relatively low temperatures, reducing drastically the volume fraction occupied by the large nuclei. With increasing temperature protons leak out of nuclei, enter the gas phase, and alter the nature of the transition to bulk matter. Here, nuclei dissolve with increasing density in a phenomenon referred to as retrograde condensation. We have introduced a new temperature, the pasta dissolution temperature $T_{\rm u}$, above which the volume fraction of nuclei cannot exceed $1/8$. At β equilibrium the dissolution temperature $T_{\rm u}^{\beta} \simeq 4 \pm 1$ MeV for EOSs with $L_{\rm sym} = 50$–60 MeV and is compatible with EFT predictions in neutron matter. The dissolution temperature $T_{\rm u}^{\beta}$ was found to decrease with increasing $L_{\rm sym}$. For matter with $Y_e > 0.2$ large nuclei and pasta persist to higher temperatures, $T_{\rm u} \simeq 15$ MeV, and retrograde condensation is absent. Our work confirms results obtained in Refs. [26,27] and expands on them by delineating the mechanism and defining a dissolution temperature $T_{\rm u}$ to provide an upper limit for any equation of state independent of finite-size corrections.

In the second part of our paper, we have analyzed the impact of coherent scattering off nuclear clusters on neutrino opacities, for thermodynamical conditions corresponding to core-collapse supernovas or neutron star mergers. We found that both the retrograde condensation and the Coulomb correlations in the static structure factor contribute to reducing the impact of coherent scattering on neutrino opacities. For matter far out of β equilibrium, where heavy nuclei and pasta persist to high temperatures, Coulomb correlations between clusters greatly reduce the coherent scattering rates at high densities. Here, rather than an increase, we found a net reduction in the opacity for thermal neutrinos when clusters are present. This may be important at very early times postbounce during the supernova when matter with a large Y_e is encountered briefly during the period when the lepton number is trapped. On longer timescales characteristic of protoneutron star evolution, β equilibrium favors much smaller values of Y_e, and for $T < T_{\rm u}^{\beta}$ only a moderate increase, by less than 20%, is found for thermal neutrinos, at variance with the factor 5 reported in Ref. [17]. We find such an increase only for high-energy nonthermal neutrinos, for which correlations between nuclei enhance the scattering rates.

While we believe that the physical effects mentioned above are robust, additional work is warranted to obtain more quantitative predictions. Hartree-Fock calculations, such as those reported in Refs. [24,52], which self-consistently include the surface tension, Coulomb, and shell effects, would provide improved estimates for $T_{\rm u}^{\beta}$ to better constrain the temperature range in which pasta is present. It will also be desirable to go beyond the single-nucleus approximation in calculating the ion structure factor and include, in addition, nonspherical shapes. Ultimately, these modifications to the neutrino opacities need to be incorporated self-consistently with the underlying equation of state in protoneutron star and supernova simulations to assess whether the presence of nuclear clusters at subnuclear densities can influence supernova observables. Nonetheless, it seems likely that retrograde condensation and ion correlations will together disfavor the large changes to the temporal structure of the neutrino signal predicted in Ref. [17].

ACKNOWLEDGMENTS

We would like to thank C. Horowitz and W. Newton for discussions. S.R. was supported by DOE Grant No. DE-FG02-00ER41132. A.R. was supported by NSF Grant No. AST-1333607 and by DOE Grant No. DE-AC52-06NA25396. L.R. was supported by the DOE Office of Science under Award No. DE-SC0017955. J.M. was partially supported by the IN2P3 Master Project MAC.

[1] A. Burrows, Rev. Mod. Phys. **85**, 245 (2013).
[2] H.-T. Janka, Annu. Rev. Nucl. Part. Sci. **62**, 407 (2012).
[3] A. Burrows and J. M. Lattimer, Astrophys. J. **307**, 178 (1986).
[4] J. A. Pons, S. Reddy, M. Prakash, J. M. Lattimer, and J. A. Miralles, Astrophys. J. **513**, 780 (1999).
[5] T. Fischer, I. Sagert, G. Pagliara, M. Hempel, J. Schaffner-Bielich, T. Rauscher, F.-K. Thielemann, R. Käppeli, G. Martínez-Pinedo, and M. Liebendörfer, Astrophys. J. Suppl. Ser. **194**, 39 (2011).
[6] L. F. Roberts and S. Reddy, in *Handbook of Supernovae*, edited by A. W. Alsabti and P. Murdin (Springer International, Cham, Switzerland, 2016), pp. 1–31.
[7] L. Hüdepohl, B. Muller, H. T. Janka, A. Marek, and G. G. Raffelt, Phys. Rev. Lett. **104**, 251101 (2010).
[8] T. Fischer, G. Martínez-Pinedo, M. Hempel, and M. Liebendörfer, Phys. Rev. D **85**, 083003 (2012).
[9] L. F. Roberts, G. Shen, V. Cirigliano, J. A. Pons, S. Reddy, and S. E. Woosley, Phys. Rev. Lett. **108**, 061103 (2012).
[10] G. Martínez-Pinedo, T. Fischer, A. Lohs, and L. Huther, Phys. Rev. Lett. **109**, 251104 (2012).
[11] S. Wanajo, ApJ **770**, L22 (2013).
[12] D. Z. Freedman, Phys. Rev. D **9**, 1389 (1974).
[13] N. K. Glendenning, Phys. Rev. D **46**, 1274 (1992).
[14] S. Reddy, G. Bertsch, and M. Prakash, Phys. Lett. B **475**, 1 (2000).
[15] C. J. Horowitz, M. A. Perez-Garcia, and J. Piekarewicz, Phys. Rev. C **69**, 045804 (2004).
[16] H. Sonoda, G. Watanabe, K. Sato, T. Takiwaki, K. Yasuoka, and T. Ebisuzaki, Phys. Rev. C **75**, 042801 (2007).
[17] C. J. Horowitz, D. K. Berry, M. E. Caplan, T. Fischer, Z. Lin, W. G. Newton, E. O'Connor, and L. F. Roberts, arXiv:1611.10226 [astro-ph.HE].
[18] N. Itoh, Prog. Theor. Phys. **54**, 1580 (1975).
[19] N. Itoh, R. Asahara, N. Tomizawa, S. Wanajo, and S. Nozawa, Astrophys. J. **611**, 1041 (2004).
[20] N. Glendenning, *Compact Stars*, 2nd ed. (Springer, Berlin, 1997).
[21] C. J. Pethick and D. G. Ravenhall, Annu. Rev. Nucl. Part. Sci. **45**, 429 (1995).
[22] F. Douchin and P. Haensel, Astron. Astrophys. **380**, 151 (2001).
[23] J. M. Pearson, N. Chamel, S. Goriely, and C. Ducoin, Phys. Rev. C **85**, 065803 (2012).
[24] W. G. Newton and J. R. Stone, Phys. Rev. C **79**, 055801 (2009).
[25] S. S. Avancini, D. P. Menezes, M. D. Alloy, J. R. Marinelli, M. M. W. Moraes, and C. Providência, Phys. Rev. C **78**, 015802 (2008).
[26] G. Watanabe, K. Sato, K. Yasuoka, and T. Ebisuzaki, Phys. Rev. C **69**, 055805 (2004); **81**, 049901(E) (2010).
[27] H. Sonoda, G. Watanabe, K. Sato, K. Yasuoka, and T. Ebisuzaki, Phys. Rev. C **77**, 035806 (2008); **81**, 049902(E) (2010).
[28] H. Muller and B. D. Serot, Phys. Rev. C **52**, 2072 (1995).
[29] S. S. Avancini, S. Chiacchiera, D. P. Menezes, and C. Providência, Phys. Rev. C **82**, 055807 (2010); **85**, 059904(E) (2012).
[30] C. Ducoin, P. Chomaz, and F. Gulminelli, Nucl. Phys. A **771**, 68 (2006).
[31] K. Huang, *Statistical Mechanics*, 2nd ed. (John Wiley & Sons, New York, 1987).
[32] I. Tews, S. Gandolfi, A. Gezerlis, and A. Schwenk, Phys. Rev. C **93**, 024305 (2016).
[33] C. Drischler, K. Hebeler, and A. Schwenk, Phys. Rev. C **93**, 054314 (2016).
[34] F. Grill, H. Pais, C. Providência, I. Vidaña, and S. S. Avancini, Phys. Rev. C **90**, 045803 (2014).
[35] W. G. Newton (unpublished) (2018).
[36] D. G. Ravenhall, C. J. Pethick, and J. R. Wilson, Phys. Rev. Lett. **50**, 2066 (1983).
[37] A. da Silva Schneider, L. F. Roberts, and C. D. Ott, Phys. Rev. C **96**, 065802 (2017).
[38] J. Lattimer, C. Pethick, D. Ravenhall, and D. Lamb, Nucl. Phys. A **432**, 646 (1985).
[39] F. Aymard, F. Gulminelli, and J. Margueron, Phys. Rev. C **89**, 065807 (2014).
[40] P. Alcain and C. Dorso, Nucl. Phys. A **961**, 183 (2017).
[41] R. F. Sawyer, Phys. Rev. D **11**, 2740 (1975).
[42] R. H. Helm, Phys. Rev. **104**, 1466 (1956).
[43] N. Desbiens, P. Arnault, and J. Clérouin, Phys. Plasmas **23**, 092120 (2016).
[44] A. L. Fetter and J. D. Walecka, *Quantum Theory of Many-Particle Systems* (Dover, Mineola, NY, 1971).
[45] N. Iwamoto and C. J. Pethick, Phys. Rev. D **25**, 313 (1982).
[46] A. Burrows and R. F. Sawyer, Phys. Rev. C **58**, 554 (1998).
[47] S. Reddy, M. Prakash, J. M. Lattimer, and J. A. Pons, Phys. Rev. C **59**, 2888 (1999).
[48] C. J. Horowitz and A. Schwenk, Phys. Lett. B **642**, 326 (2006).
[49] C. J. Horowitz, O. L. Caballero, Z. Lin, E. O'Connor, and A. Schwenk, Phys. Rev. C **95**, 025801 (2017).
[50] C. J. Horowitz, Phys. Rev. D **55**, 4577 (1997).
[51] M. Onsi, A. K. Dutta, H. Chatri, S. Goriely, N. Chamel, and J. M. Pearson, Phys. Rev. C **77**, 065805 (2008).
[52] B. Schuetrumpf, C. Zhang, and W. Nazarewicz, in *Nuclear Particle Correlations and Cluster Physics*, edited by W.-U. Schröder (World Scientific, Singapore, 2017), pp. 135–153